arXiv:2604.25371v2 [q-bio.QM] 15 Jun 2026

PhyloSDF: Phylogenetically-Conditioned Neural Generation of 3D Skull Morphology via Residual Flow Matching

Kaikwan Lau
Department of Mathematics
The Chinese University of Hong Kong
kaikwan.lau@link.cuhk.edu.hk

Gary P. T. Choi
Department of Mathematics
The Chinese University of Hong Kong
ptchoi@cuhk.edu.hk

Abstract

Generating novel, biologically plausible three-dimensional morphological structures is a fundamental challenge in computational evolutionary biology, hampered by extreme data scarcity and the requirement that generated shapes respect phylogenetic relationships among species. In this work, we present PhyloSDF, a phylogenetically-conditioned neural generative model for 3D biological morphology that integrates two innovations: (1) a DeepSDF auto-decoder regularized by a novel Phylogenetic Consistency Loss that structures the latent space to correlate with evolutionary distances (Pearson $r = 0.993$); (2) a Residual Conditional Flow Matching (Residual CFM) architecture that factorizes generation into analytic species-centroid lookup and learned residual prediction, enabling generation from as few as ~ 4 specimens per species. We evaluate PhyloSDF on 100 micro-CT-scanned skulls of Darwin's Finches and their relatives across 24 species. The model generates novel meshes achieving 88–129% of real intra-species variation at the code level, with all 180 generated meshes verified as non-memorized. Residual CFM surpasses denoising diffusion (which fails entirely at this scale), standard flow matching (which mode-collapses to 3–6% variation), and a Gaussian mixture baseline in both fidelity (Chamfer Distance 0.00181 vs. 0.00190) and morphometric Fréchet distance (10,641 vs. 13,322). Leave-one-species-out experiments across 18 species demonstrate phylogenetic extrapolation capability, and smooth latent interpolations produce biologically plausible ancestral skull reconstructions.

***K*eywords** Generative Modelling · Signed Distance Functions · Flow Matching · Phylogenetics · 3D Morphology · Darwin's Finches

1 Introduction

Three-dimensional morphological data lie at the heart of comparative biology, paleontology, and evolutionary developmental biology [1, 2, 3]. The advent of high-resolution micro-computed tomography (μCT) has made it possible to digitize biological specimens as dense 3D surface meshes [4], allowing quantitative morphometric analyses at unprecedented geometric detail [5]. However, morphological datasets remain remarkably small by the standards of modern machine learning: a typical study encompasses tens to at most a few hundred specimens, limited by the availability of museum material [6], the cost of scanning, and labor-intensive segmentation and quality control.

This data scarcity poses a fundamental obstacle for deep generative modeling. State-of-the-art generative frameworks, such as variational autoencoders [7], generative adversarial networks [8], denoising diffusion probabilistic models (DDPM) [9], and flow matching [10], have demonstrated extraordinary results on images and 3D shapes, but invariably assume access to thousands to millions of training samples. When naively applied to scientific datasets with only a few hundred or even fewer samples, these models either diverge during training, collapse to trivial point estimates, or memorize the training set [11], yielding not merely

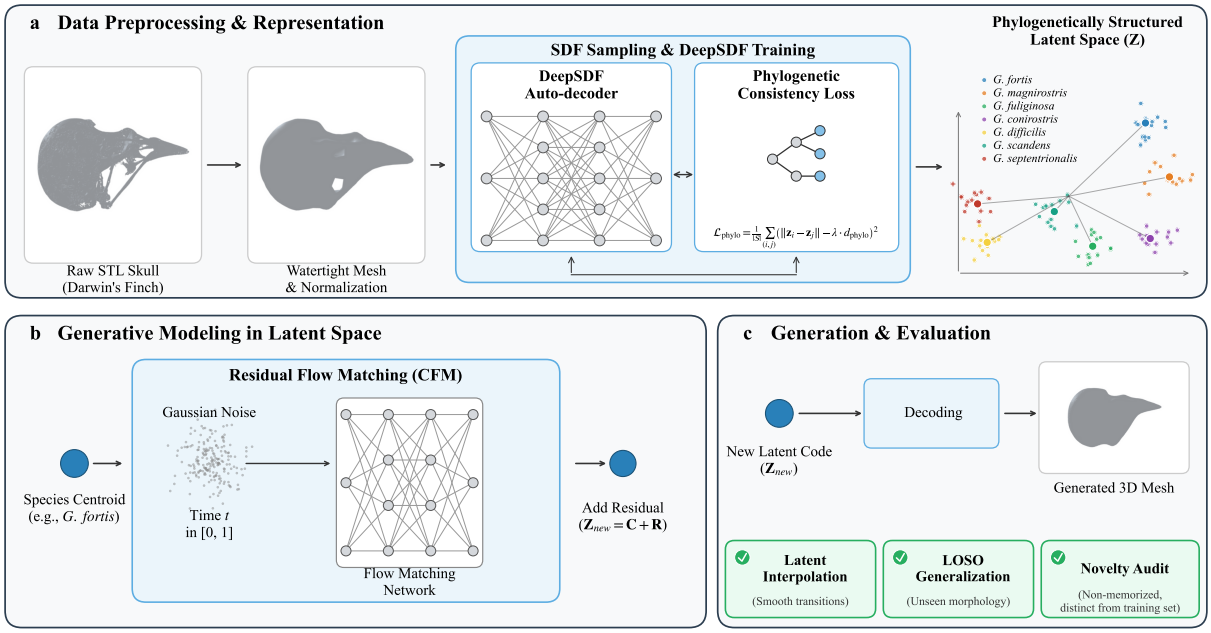

Figure 1: **Overview of the proposed pipeline for phylogenetically-conditioned 3D skull generation.** (a) Data preprocessing and representation. Raw STL skull meshes from museum specimens of Darwin's Finches and their relatives are converted to watertight meshes and normalized, after which signed distance function (SDF) samples are generated for DeepSDF auto-decoder training. A Phylogenetic Consistency Loss augments the standard DeepSDF objective by maximizing the Pearson correlation between pairwise Euclidean distances in the latent code library and pairwise phylogenetic distances derived from genus-level taxonomy, producing a continuously structured latent space in which evolutionary proximity is reflected by geometric proximity. (b) Generative modeling in latent space. A Residual Conditional Flow Matching (CFM) network learns to generate intra-species residuals, deviations of individual latent codes from their species centroid, rather than full latent codes directly. Given a target species centroid as conditioning, the network integrates a learned velocity field from Gaussian noise over the unit time interval, and the resulting residual is added back to the centroid to produce a new latent code. (c) Generation and evaluation. New latent codes are decoded by the frozen DeepSDF decoder into full 3D skull meshes. The framework is evaluated along three axes: latent interpolation between species centroids to assess smoothness of the learned manifold; a leave-one-species-out (LOSO) protocol that predicts held-out species morphology from phylogenetically neighboring taxa; and a novelty audit confirming that generated meshes are distinct from all training specimens as measured by the Chamfer Distance.

unhelpful but potentially scientifically misleading outcomes [12]. Beyond data volume, biological morphology introduces a structural constraint absent from conventional generative settings, phylogenetic coherence [13], in which species are connected by an evolutionary tree constraining their morphological similarity. Any generative model intended for biological applications must respect this phylogenetic structure, which reflects the fundamental process of descent with modification and is indispensable for applications such as ancestral state reconstruction.

Our work is driven by the question: *Can we build a neural generative model that produces novel, biologically plausible 3D specimens for species with very few available scans, while respecting evolutionary relationships?* Such a model would enable virtual specimen augmentation for morphometric studies, hypothesis testing via ancestral reconstruction, and predictive modeling of morphological evolution. Achieving this goal requires overcoming several intertwined difficulties. The most fundamental is extreme data scarcity, with approximately four specimens per species in a 64-dimensional latent space, the sample-to-dimension ratio is barely above unity, and standard generative models invariably collapse to the species mean [14]. Compounding this, each specimen is a dense, high-resolution watertight mesh with 50K–140K vertices, so the generative model must produce latent codes that decode through a neural signed distance field into anatomically plausible 3D surfaces,

not merely plausible statistics. A third challenge is unique to biological data: the learned representation must encode *phylogenetic structure*, organizing species in latent space according to their evolutionary relationships rather than treating them as independent classes. Finally, on datasets of this scale, any claim of genuine "generation" demands rigorous verification that outputs are truly novel rather than memorized or trivially interpolated copies of training specimens, a concern that standard metrics such as Fréchet Inception Distance cannot address when the reference set contains only 100 shapes [15].

In this work, we introduce PhyloSDF, a phylogenetically conditioned neural generative model for 3D biological morphology that addresses all of the aforementioned challenges. Figure 1 illustrates the complete PhyloSDF pipeline, which maps raw micro-CT meshes into a phylogenetically structured latent space, factorizes generative modeling via Residual Flow Matching, and employs domain-specific evaluation metrics to ensure biological validity.

Our first contribution is the development of a **Phylogenetic Consistency Loss**, a novel regularization that constrains the geometry of the learned shape manifold to reflect evolutionary relationships. By integrating this regularization into DeepSDF [16], we can get a latent space in which morphological and phylogenetic distances are correlated by construction, achieving a Pearson correlation of $r = 0.993$.

Another significant contribution is **Residual Conditional Flow Matching** (Residual CFM), a novel generative architecture that factorizes the generation task into two complementary components: an analytic species-centroid lookup that handles species identity, and a neural residual flow that captures intra-species variation. The key insight is that by subtracting species centroids and pooling the resulting residuals across all 100 specimens, it explicitly separates taxonomic identity from individual variation. This residual decomposition transforms what would otherwise be 24 separate learning problems, each with approximately four training examples, into a single conditionally-shared distribution over intra-species variation fit to all 100 specimens simultaneously, not by increasing the number of training points, but by restructuring the learning target so that all specimens, regardless of species, contribute evidence about the same quantity that is the shape and scale of within-species morphological deviation from a species mean.

Finally, we introduce an evaluation framework for phylogenetically-conditioned biological shape generation comprising three components: (i) the Latent Phylogenetic Consistency (LPC) score, which measures the Pearson correlation between pairwise latent distances and pairwise phylogenetic distances to quantify how well evolutionary relationships are preserved in the learned shape manifold; (ii) Morphometric FID (MorphFID), a Fréchet distance computed over interpretable geometric descriptors including surface area, volume, bounding-box extents, and compactness, that provides a distribution-level quality score without requiring a domain-specific pretrained network; and (iii) a leave-one-species-out protocol that evaluates phylogenetic extrapolation by predicting held-out species centroids from phylogenetically neighboring taxa and measuring proximity to real specimens in latent space. These metrics address the specific challenges of evaluating generative models on small biological datasets where standard metrics such as Fréchet distance (FID) [17] and coverage are unreliable [15].

Together, these contributions provide a robust pipeline for evolutionary shape modeling. In the following, we first review the related works in biological shape representation and generation. Then, we formalize the underlying mechanics of PhyloSDF, beginning with our problem setting and mathematical formulation.

2 Related Work

2.1 Neural Implicit 3D Representations

Implicit neural representations have become the dominant paradigm for continuous 3D shape encoding. DeepSDF [16] introduced the auto-decoder architecture in which a shared neural network maps a latent code and a 3D query point to a signed distance value, enabling smooth surface reconstruction at arbitrary resolution and supporting direct latent-space interpolation without an encoder network. Occupancy Networks [18] proposed an alternative binary occupancy formulation that relaxes the Eikonal constraint while preserving resolution-independence. IM-NET [19] demonstrated that implicit decoders can be conditioned on global shape embeddings to generate diverse shapes from compact codes. Subsequent work on Neural Unsigned Distance Fields [20] and Implicit Differentiable Renderer [21] extended these ideas to open surfaces and appearance modeling, respectively. PhyloSDF builds directly on the DeepSDF auto-decoder architecture, extending it with a phylogenetic consistency loss that structures the latent space geometrically according to evolutionary relationships, a constraint that prior implicit representation methods do not consider.

2.2 Generative Models for 3D Shapes

Generative modeling of 3D geometry has been approached across a spectrum of representations. Point-cloud methods [22, 23] use variational autoencoders or normalizing flows to model unstructured point sets, while voxel-based approaches [24] apply 3D convolutional architectures to occupancy grids but suffer from cubic memory scaling. Mesh-based generative models [25] have demonstrated sequential generation of triangle meshes, though they require fixed mesh topology. For neural implicit representations specifically, DualSDF [26] introduced generative frameworks operating in the latent spaces of implicit decoders. More recent work has applied DDPM [9] to 3D shape latents [27], achieving high-quality results on large-scale datasets such as ShapeNet with tens of thousands of training examples. Flow matching [10] has emerged as a more training-stable alternative, demonstrated on both image and shape generation at scale.

A common thread across all these methods is the assumption of dataset sizes in the range of 10^3 to 10^6 examples; their training dynamics, architectural choices, and evaluation protocols are calibrated for this regime. When applied naively to datasets of $N \sim 100$ specimens, these models invariably collapse to per-class means or memorize the training set [11]. PhyloSDF is specifically designed for this extreme-scarcity regime. While the method is taxon-agnostic in design, all experiments in this paper are conducted on the skull morphology of Darwin's Finches and their relatives. Generalization to other taxa remains a direction for future work.

2.3 Phylogenetic Comparative Methods and Machine Learning

Incorporating phylogenetic information into machine learning has been explored in several related contexts. Phylogenetic signal has been used as a feature for trait prediction [28] and species classification [29]. Pagel's λ [30] and related statistics quantify the degree to which trait covariance matches the expectation from a known phylogeny, but these methods operate on scalar or low-dimensional trait vectors rather than on neural latent representations. To our knowledge, no prior work has used phylogenetic patristic distances as a regularizer on the geometry of a neural shape representation, nor has any previous method proposed a quantitative metric, analogous to our Latent Phylogenetic Consistency score, for measuring evolutionary coherence in a learned latent space.

The preceding survey reveals a consistent gap: no existing method jointly addresses extreme data scarcity, phylogenetic structure, and full 3D morphological generation. Methods from geometric morphometrics lack generative capacity; 3D generative models assume large datasets and ignore evolutionary relationships; and phylogenetic comparative methods operate on low-dimensional trait vectors rather than neural shape representations. Our proposed PhyloSDF method addresses all three challenges simultaneously through a phylogenetically-regularized auto-decoder, a residual flow matching architecture designed for the $N \sim 100$ regime, and a biologically-informed evaluation framework.

3 Mathematical Background

We establish the mathematical foundations upon which PhyloSDF is built. First, we cover the mathematical background of our method. Then, we introduce the generative and evaluation frameworks we build upon.

3.1 Implicit Surface Representation

Let $\Omega \subset \mathbb{R}^3$ be a compact region with C^1 boundary $\partial\Omega$. The signed distance function (SDF) [31] encodes the geometry of $\partial\Omega$ as a scalar field:

$$\phi_\Omega(\mathbf{p}) \;=\; \operatorname{sgn}(\mathbf{p}) \inf_{\mathbf{q}\,\in\,\partial\Omega} \|\mathbf{p}-\mathbf{q}\|_2, \tag{1}$$

where $\operatorname{sgn}(\mathbf{p}) = \begin{cases} -1, & \mathbf{p} \in \Omega, \\ +1, & \mathbf{p} \notin \Omega, \end{cases}$, so that $\partial\Omega$ is recovered as the zero level-set $\{\mathbf{p} \in \mathbb{R}^3 : \phi_\Omega(\mathbf{p}) = 0\}$. A key property is $\|\nabla\phi_\Omega\|_2 = 1$ almost everywhere (the Eikonal condition), which constrains the geometry of valid SDFs [32].

DeepSDF [16] parameterizes the mapping ϕ_Ω with a neural network $f_\theta : \mathbb{R}^D \times \mathbb{R}^3 \to \mathbb{R}$, taking a latent code $\mathbf{z} \in \mathbb{R}^D$ and a query point $\mathbf{p} \in \mathbb{R}^3$ as input. In the auto-decoder formulation, each training specimen i owns a dedicated learnable code $\mathbf{z}_i$, optimized jointly with the shared decoder weights θ by minimizing

$$\mathcal{L}_{\text{rec}}(\theta, \{\mathbf{z}_i\}) = \frac{1}{|\mathcal{P}_i|} \sum_{\mathbf{p}\in\mathcal{P}_i} \Big| \operatorname{clamp}_\delta\big(f_\theta(\mathbf{z}_i, \mathbf{p})\big) - \operatorname{clamp}_\delta\big(\phi_i(\mathbf{p})\big) \Big|, \tag{2}$$

where $\phi_i(\mathbf{p})$ is the ground-truth signed distance for specimen i, $\text{clamp}_\delta(x) = \max(-\delta, \min(\delta, x))$ with $\delta = 0.1$ suppresses the influence of far-field points, and $\mathcal{P}_i$ is a set of 5×10^4 query points per specimen sampled from a half-half mixture of surface-proximal ($\|\mathbf{p}\|_2 < 0.1$ from $\partial\Omega_i$).

Note that the auto-decoder architecture decouples shape representation from any encoder, making it directly amenable to the latent-space generative modeling in Section 4. Each $\mathbf{z}_i \in \mathbb{R}^{64}$ is a complete implicit encoding of specimen i's 3D morphology; there is no separate encoding step at generation time.

3.2 Phylogenetic Distance

A phylogenetic tree $\mathcal{T} = (V, E, \ell)$ is a rooted, edge-weighted tree in which leaves correspond to extant taxa, internal nodes correspond to hypothetical common ancestors, and $\ell : E \to \mathbb{R}_{>0}$ assigns evolutionary time (or molecular divergence) to each branch. We define the Patristic Distance $d_{\text{phylo}}(a, b)$ between taxa a, b as the total branch length along the unique path connecting them in $\mathcal{T}$:

$$d_{\text{phylo}}(a, b) \;=\; \sum_{e \,\in\, \text{path}(a,b)} \ell(e). \tag{3}$$

In practice, we use a genus-level proxy derived from published molecular phylogenies of the Thraupidae [33, 34], assigning normalized distances as follows: $d = 0.125$ for congeneric species; $d = 0.375$ for sister genera within a tribe; $d = 1.0$ for pairs spanning the root. All distances are normalized to $[0, 1]$.

3.3 Flow Matching

Flow matching [10, 35] learns a generative model as a continuous normalizing flow defined by a learned velocity field. Let $p_0 = \mathcal{N}(\mathbf{0}, \mathbf{I}_D)$ be a tractable source distribution and p_1 be the target data distribution over $\mathbb{SR}^D$. The goal is to learn a time-dependent velocity field $v_\theta : \mathbb{R}^D \times [0, 1] \to \mathbb{R}^D$ such that integrating the ODE

$$\frac{d\mathbf{x}_t}{dt} \;=\; v_\theta(\mathbf{x}_t,\, t), \qquad \mathbf{x}_0 \sim p_0, \tag{4}$$

from $t = 0$ to $t = 1$, transports p_0 to p_1. Direct optimization of Eq. (4) is intractable because the marginal velocity is not available in closed form. The conditional flow matching (CFM) objective [10] circumvents this by conditioning on individual data points. The Conditional Flow Matching Loss function is defined as follows. Given $\mathbf{x}_0 \sim p_0$ and target sample $\mathbf{x}_1 \sim p_1$, sampled independently, we first define the straight-line conditional path

$$\mathbf{x}_t \;=\; (1 - t)\,\mathbf{x}_0 + t\,\mathbf{x}_1, \tag{5}$$

with conditional target velocity $u_t(\mathbf{x}_t \mid \mathbf{x}_1) = \mathbf{x}_1 - \mathbf{x}_0$. The CFM training objective is then defined as

$$\mathcal{L}_{\text{CFM}} \;=\; \mathbb{E}_{t\sim\mathcal{U}[0,1],\, \mathbf{x}_0\sim p_0,\, \mathbf{x}_1\sim p_1} \Big\| v_\theta(\mathbf{x}_t,\, t) \;-\; (\mathbf{x}_1 - \mathbf{x}_0) \Big\|_2^2. \tag{6}$$

It was shown in [10] that minimizing $\mathcal{L}_{\text{CFM}}$ is equivalent to minimizing the marginal flow matching objective, so that training on independent sample pairs $(\mathbf{x}_0, \mathbf{x}_1)$ recovers the correct population-level transport map. In conclusion, Eq. (4) is solved by $K = 50$ Euler steps with step size $\Delta t = 1/K$.

The straight-line interpolant in Eq. (5) uses independent coupling between p_0 and p_1; this is distinct from OT-CFM [36], which minimizes transport cost by pairing source and target samples. The independent formulation is deliberate: with only $N \sim 100$ training samples, estimating the OT coupling is statistically unreliable and would introduce additional variance. More broadly, the single-ODE structure of flow matching contrasts with the 1,000-step Markov chain of DDPM [9], whose per-step approximation errors compound multiplicatively and render it numerically unstable at this data scale (see Section 5).

3.4 Fréchet Distance between Gaussian Distributions

Let $P_k = \mathcal{N}(\boldsymbol{\mu}_k, \boldsymbol{\Sigma}_k)$, $k = 1, 2$, be two distributions on $\mathbb{R}^d$. The squared Fréchet distance, equivalently, the squared 2-Wasserstein distance between Gaussians [37] admits the closed-form expression

$$d_F^2(P_1, P_2) = \|\boldsymbol{\mu}_1 - \boldsymbol{\mu}_2\|_2^2 + \text{tr}\Big(\boldsymbol{\Sigma}_1 + \boldsymbol{\Sigma}_2 - 2\left(\boldsymbol{\Sigma}_1^{1/2}\boldsymbol{\Sigma}_2\boldsymbol{\Sigma}_1^{1/2}\right)^{1/2}\Big), \tag{7}$$

where $(\cdot)^{1/2}$ denotes the unique symmetric positive semidefinite matrix square root. The FID [17] instantiates Eq. (7) with $\boldsymbol{\mu}_1, \boldsymbol{\mu}_2 \in \mathbb{R}^d$ and $\boldsymbol{\Sigma}_1, \boldsymbol{\Sigma}_2 \in \mathbb{R}^{d\times d}$ are mean vectors and the covariance matrices estimated from Inception network activations respectively.

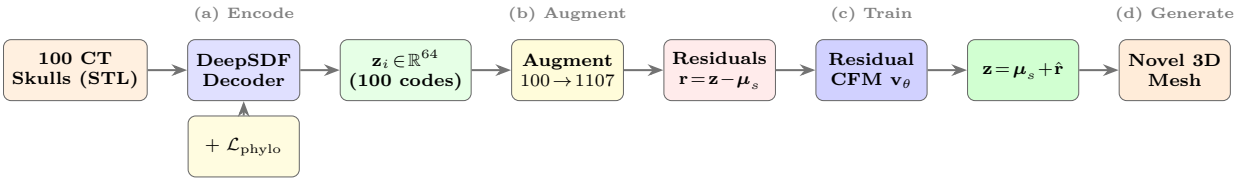

Figure 2: **Overview of our PhyloSDF pipeline.** (a) DeepSDF auto-decoder learns $\mathbf{z}_i$ with phylogenetic consistency loss. (b) Latent augmentation expands codes. (c) Residual CFM learns noise, then residual mapping. (d) Generation: $\mathbf{z}_{\text{new}} = \boldsymbol{\mu}_s + \text{CFM}(\boldsymbol{\epsilon})$, decoded via Marching Cubes.

Note that there are two fundamental obstacles that prevent the direct application of FID to biological morphology. First, Inception features carry no semantic meaning for 3D skull meshes, rendering the resulting distance geometrically uninterpretable. Second, reliable estimation of a $d \times d$ covariance matrix via the sample covariance requires $n \gg d$ observations; with $N = 100$ specimens and a typical Inception feature dimension $d \sim 2{,}048$, the sample covariance is severely rank-deficient. Our MorphFID metric (Section 5.10) avoids both problems by replacing Inception activations with a low-dimensional vector of interpretable morphometric descriptors.

3.5 Chamfer Distance

For point clouds $P, Q \subset \mathbb{R}^3$, the Chamfer distance is given by

$$\text{CD}(P, Q) = \frac{1}{|P|} \sum_{\mathbf{p} \in P} \min_{\mathbf{q} \in Q} \|\mathbf{p} - \mathbf{q}\|_2^2 + \frac{1}{|Q|} \sum_{\mathbf{q} \in Q} \min_{\mathbf{p} \in P} \|\mathbf{q} - \mathbf{p}\|_2^2. \tag{8}$$

The foundations established above, implicit shape encoding via the auto-decoder, phylogenetic distance as a geometric prior, and flow matching as a generative framework, are combined and extended in Section 4.

4 Method

PhyloSDF comprises three stages (Fig. 2): (1) Phylogenetically-regularized DeepSDF encoding; (2) Biologically-informed latent space augmentation; and (3) Residual CFM training and generation. Stages 1 and 3 introduce novel components; Stage 2 bridges the extreme data scarcity between them.

4.1 Stage 1: Phylogenetically-Regularized DeepSDF

We adopt the DeepSDF auto-decoder formulation, in which each of the $N = 100$ specimens owns a learnable latent code $\mathbf{z}_i \in \mathbb{R}^{64}$ optimized jointly with the shared decoder f_θ via the reconstruction objective $\mathcal{L}_{\text{rec}}$ defined in Eq. (2). We extend this objective with a novel **Phylogenetic Consistency Loss** that structures the latent space geometrically according to evolutionary history.

The key observation is that under Brownian motion trait evolution, the expected squared morphological divergence between two taxa is proportional to their patristic distance $d_{\text{phylo}}(a, b)$ [33, 34]. We enforce this property directly in the learned latent space by maximizing the Pearson correlation between the vector of all pairwise latent code distances and the corresponding vector of pairwise phylogenetic distances. Let $\mathcal{S}$ be a random subset of specimen pairs (i, j) sampled every 10 training batches, and $d_{ij}^L = \|\mathbf{z}_i - \mathbf{z}_j\|_2$ and $d_{ij}^P = d_{\text{phylo}}(a_i, b_j)$ denote the latent and phylogenetic distances respectively. The loss is:

$$\mathcal{L}_{\text{phylo}} = -\,\rho\big(\{d_{ij}^L\}_{(i,j)\in\mathcal{S}},\ \{d_{ij}^P\}_{(i,j)\in\mathcal{S}}\big)\,, \tag{9}$$

where $\rho(\cdot, \cdot)$ is the Pearson correlation coefficient. Minimizing $\mathcal{L}_{\text{phylo}}$ is equivalent to maximizing the linear alignment between morphological and phylogenetic pairwise distances, making the loss differentiable and directly interpretable via the same LPC metric used at evaluation time. The full DeepSDF objective is:

$$\mathcal{L}_{\text{DeepSDF}} = \mathcal{L}_{\text{rec}} + \alpha \|\mathbf{z}_i\|_2^2 + \beta\, \mathcal{L}_{\text{phylo}}, \tag{10}$$

with $\alpha = 10^{-3}$ and $\beta = 0.5 \times 10^{-3}$. The phylogenetic loss is activated every 10 batches to reduce computational overhead; between activations, only $\mathcal{L}_{\text{rec}}$ and the ℓ_2 regularizer are used. Figure 3 illustrates the phylogenetic

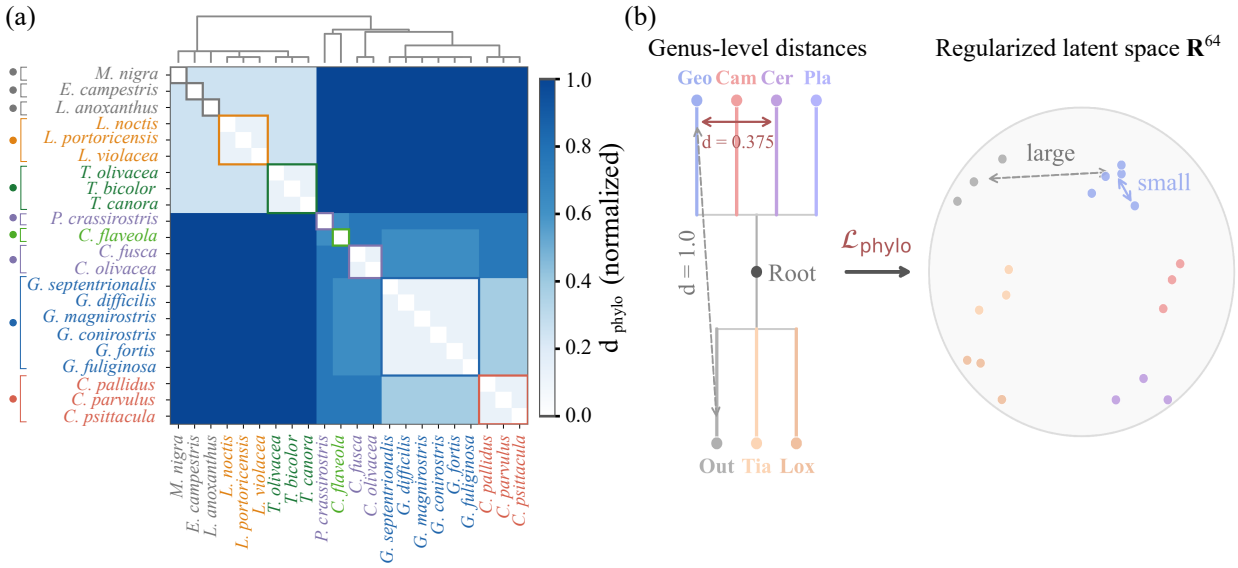

Figure 3: **The phylogenetic structure that drives the phylogenetic consistency loss in our formulation.** (a) Normalized pairwise phylogenetic distance matrix d_{phylo} for all species in the dataset, with genus-level color coding and hierarchical clustering dendrogram. Colored boxes highlight intra-genus blocks. (b) The phylogenetic consistency loss $\mathcal{L}_{\text{phylo}}$ maps genus-level tree distances into the regularized latent space $\mathbb{R}^{64}$.

structure that drives $\mathcal{L}_{\text{phylo}}$: the schematic shows how genus-level tree distances are mapped into the regularized latent space, and the heatmap shows the full distance matrix whose pairwise values serve as both the training target and the LPC evaluation ground truth. Closely related genera (e.g. *Geospiza–Camarhynchus*, $d = 0.375$) occupy nearby latent regions; distantly related outgroup species (grey) are pushed far from the Darwin's Finches clade.

4.2 Stage 2: Latent Space Augmentation

Given the limited training set of ~ 100 specimens. Direct generative modeling is statistically infeasible, as the covariance matrix is severely rank-deficient and per-species subsets contain only ~ 4 points. We address this through three complementary augmentation strategies, each grounded in biological reasoning, that collectively expand the training set from hundreds to thousands while preserving the geometry and conditioning structure of the latent manifold.

4.2.1 PCA-Guided Perturbation

We perturb each training code along the principal axes of the global latent covariance, scaling noise magnitude by the square root of each eigenvalue so that perturbations remain proportional to the observed variance in each direction. Let $\mathbf{V} \in \mathbb{R}^{D\times D}$ be the eigenvector matrix of $\text{Cov}(\{\mathbf{z}_i\})$ with corresponding eigenvalues $\{\lambda_k\}$. For each specimen i, we generate $m = 5$ augmented codes:

$$\mathbf{z}'_i = \mathbf{z}_i + \mathbf{V}\,(\boldsymbol{\epsilon} \odot \sqrt{\boldsymbol{\lambda}}), \quad \boldsymbol{\epsilon} \sim \mathcal{N}(\mathbf{0}, \sigma^2\mathbf{I}), \tag{11}$$

where $\sigma = 0.3$ and $\boldsymbol{\lambda} = (\lambda_1, \ldots, \lambda_D)^\top$. This keeps augmented codes within the observed data manifold, unlike isotropic Gaussian noise in the ambient $\mathbb{R}^{64}$, where almost all volume is off-manifold. This strategy produces 500 additional codes.

4.2.2 Phylogenetic Interpolation

For each pair of species (a, b) with the normalized phylogenetic distance $d_{\text{phylo}}(a, b) \leq 0.7$, we draw one representative specimen from each species and generate $n = 5$ linearly interpolated codes:

$$\mathbf{z}_{\text{interp}} = (1 - \alpha)\,\mathbf{z}_i + \alpha\,\mathbf{z}_j, \tag{12}$$

where $\alpha \in \text{linspace}(0.1,\ \max(0.2,\ 0.5 - 0.3\, d_{\text{phylo}}(a,b)),\ n)$. The upper bound on α decreases linearly with phylogenetic distance: closely related species permit interpolation up to the midpoint of their latent vectors, while distant pairs are constrained to stay near the anchor species. Species pairs with $d_{\text{phylo}} > 0.7$ are excluded entirely, ensuring that only biologically plausible intermediates are synthesized. Bounding box dimensions are interpolated in parallel to preserve size conditioning consistency. This strategy produces 435 additional codes.

4.2.3 Centroid Extrapolation

Each species centroid $\boldsymbol{\mu}_s$ is extrapolated along its displacement direction from the global mean $\bar{\mathbf{z}}$:

$$\mathbf{z}_{\text{extrap}} = \boldsymbol{\mu}_s + \gamma\,(\boldsymbol{\mu}_s - \bar{\mathbf{z}}), \quad \gamma \in \{0.3,\ 0.5,\ 0.7\}, \tag{13}$$

generating three codes per species that explore the periphery of each species' realized morphospace without crossing into neighboring species' territories. This strategy produces 72 additional codes.

The three strategies yield 1,107 total codes (100 original +500 + 435 + 72). During subsequent CFM training, original specimens receive 3× upweighted sampling via a weighted random sampler, ensuring that augmented codes supplement rather than dilute the real training signal.

4.3 Stage 3: Residual Conditional Flow Matching

When standard conditional flow matching is applied directly to the latent codes, each species provides few target points in $\mathbb{R}^{64}$. Because $\mathcal{L}_{\text{CFM}}$ is a mean-squared-error loss, the MSE-optimal velocity field given so few conditioning examples converges to the conditional expectation, i.e., the species centroid, and the model fails to capture any within-species variation. Our experiments confirm this: standard CFM achieves only 3–6% of real intra-species variation (see Section 5). This failure is not a hyperparameter issue but a fundamental consequence of the sample-to-dimension ratio in the conditioned subspace.

Our solution exploits the group structure of the data. We decompose each latent code into its species centroid and a residual:

$$\mathbf{z}_i = \boldsymbol{\mu}_{s(i)} + \mathbf{r}_i, \qquad \boldsymbol{\mu}_s = \frac{1}{|S_s|} \sum_{j \in S_s} \mathbf{z}_j, \tag{14}$$

where $s(i)$ is the species i, S_s is the set of specimens belonging to species s, $|S_s|$ is the cardinality of the set S_s, $\mathbf{r}_i$ is the intra-species residual of specimen i, and $\boldsymbol{\mu}_s$ is the species centroid and train the CFM to generate normalized residuals $\tilde{\mathbf{r}}_i = (\mathbf{r}_i - \boldsymbol{\mu}_r)/\sigma_r$. $\boldsymbol{\mu}_r$ and σ_r are the global residual mean and scalar standard deviation computed from the augmented training set. Note that $\boldsymbol{\mu}_s$ is computed analytically from real codes only and requires no learning.

The key insight is that all residuals are zero-centered regardless of species identity. The network learns one quantity well from abundant examples, the shape and scale of within-species morphological deviation from a species mean, rather than attempting to learn 24 separate quantities from four examples each.

A residual CFM trained with the standard objective alone can still exhibit variance collapse, generating residuals with negligible magnitude. To prevent this, we augment $\mathcal{L}_{\text{CFM}}$ with a variance-preservation penalty:

$$\mathcal{L}_{\text{var}} = \max(0,\ \text{Var}(\mathbf{x}_1) - \text{Var}(\hat{\mathbf{x}}_1))\,, \tag{15}$$

where $\hat{\mathbf{x}}_1 = \mathbf{x}_{0.5} + 0.5\, v_\theta(\mathbf{x}_{0.5}, 0.5)$ is a one-step estimate of the generated output evaluated at the trajectory midpoint. The total training objective is

$$\mathcal{L} = \mathcal{L}_{\text{CFM}} + \lambda_v\, \mathcal{L}_{\text{var}}, \quad \lambda_v = 0.1. \tag{16}$$

4.4 Generation Procedure

Given a target species s with centroid $\boldsymbol{\mu}_s$ and phylogenetic embedding $\boldsymbol{\phi}_s$, new skull meshes are generated as follows: (i) sample $\mathbf{x}_0 \sim \mathcal{N}(\mathbf{0}, \mathbf{I}_{64})$; (ii) integrate the learned velocity field from $t = 0$ to $t = 1$ using $K = 50$ Euler steps with step size $\Delta t = 1/K$; (iii) denormalize the output residual $\hat{\mathbf{r}} = \mathbf{x}_1 \cdot \sigma_r + \boldsymbol{\mu}_r$; (iv) reconstruct the full latent code $\mathbf{z}_{\text{new}} = \boldsymbol{\mu}_s + \hat{\mathbf{r}}$; and (v) decode $\mathbf{z}_{\text{new}}$ via Marching Cubes on a 256^3 voxel grid (see SI Section S1 for a summary of the procedure).

With the above generation procedure, we can achieve ancestral reconstruction. Specifically, given two extant species a and b, the morphology of their hypothetical common ancestor is reconstructed by interpolating both centroids and phylogenetic embeddings:

$$\boldsymbol{\mu}_{\text{anc}} = \tfrac{1}{2}(\boldsymbol{\mu}_a + \boldsymbol{\mu}_b), \qquad \boldsymbol{\phi}_{\text{anc}} = \tfrac{1}{2}(\boldsymbol{\phi}_a + \boldsymbol{\phi}_b), \tag{17}$$

and then sampling residuals conditioned on $(\boldsymbol{\mu}_{\text{anc}}, \boldsymbol{\phi}_{\text{anc}})$ via the generation procedure above.

The three-stage pipeline described above, phylogenetically-regularized encoding (Stage 1), biologically-informed augmentation (Stage 2), and residual flow matching (Stage 3), constitutes the complete PhyloSDF framework. The velocity network used within the Residual Conditional Flow Matching stage of the broader PhyloSDF framework is further referred to as **PhyloFlowNet**.

5 Experiments

This section describes the experimental instantiation of this framework, including dataset details, implementation settings, and quantitative evaluation against baseline methods. More details of the training hyperparameters, optimizer configurations, and network architectures for both the DeepSDF decoder and PhyloFlowNet are provided in SI Section S1 and Table S1–S2.

5.1 Dataset

We focus on the dataset of Darwin's Finches and their relatives from [38, 39, 40], which comprises $N = 100$ micro-CT skull specimens drawn from 24 avian species spanning Darwin's Finches radiation and its closest relatives (Fig. 4). The core Darwin's Finches clade, including *Geospiza*, *Camarhynchus*, *Certhidea*, *Platyspiza*, and *Pinaroloxias*, contributes 53 specimens across 14 species. The remaining 47 specimens span 10 species of close relatives and outgroups from the families *Thraupidae* (tanagers) and *Emberizidae* are included to provide phylogenetically distant reference points that anchor the latent space geometry learned by $\mathcal{L}_{\text{phylo}}$. All specimens were acquired as watertight STL meshes and preprocessed into SDF samples as described in Section 3. We apply the voxelization and smoothing procedure as described in [40] to remesh the original 3D scans (see Fig. 1(a) for an illustration).

It is noteworthy that the dataset is severely class-imbalanced: specimen counts per species range from 2 (*G. difficilis*, *G. septentrionalis*, *P. inornata*, *C. fusca*) to 7 (*G. conirostris*), with a mean of 4.2 specimens per species. This imbalance is not an artifact of sampling effort but reflects the genuine scarcity of museum specimens for rare or island-endemic species. The augmentation pipeline in Section 4 is motivated by this constraint: no species has enough specimens to fit a meaningful per-species generative model without augmentation.

Normalized phylogenetic distances are assigned at several levels following the genus-level taxonomy of [33, 34]: congeneric species pairs receive $d_{\text{phylo}} = 0.125$, sister genera receive $d_{\text{phylo}} = 0.375$, and all remaining pairs, including outgroup comparisons, receive $d_{\text{phylo}} = 1.0$. These distances are used without modification as the training target for $\mathcal{L}_{\text{phylo}}$.

5.2 Baselines

We compare the proposed Residual CFM against three baselines that span the spectrum from classical statistics to deep generative modeling. The first is DDPM, a denoising diffusion probabilistic model with 1,000 denoising steps and the same multi-modal conditioning architecture used by our method; this baseline tests whether iterative denoising can function at this data scale. The second is Standard CFM, which applies conditional flow matching directly to the full latent codes without residual decomposition, thereby isolating the contribution of our residual factorization. The third is a non-neural Gaussian Mixture Model (GMM) that fits a per-species Gaussian with Ledoit-Wolf covariance shrinkage. This serves as a strong statistical baseline that requires no training and provides a lower bound on what simple distributional modeling can achieve. The proposed **Residual CFM** combines all three of our innovations: phylogenetic consistency loss, latent augmentation, and residual flow matching.

5.3 Evaluation Metrics

All metrics are computed on 10K-point clouds sampled from generated and training meshes, with both sets normalized to the unit cube to ensure scale-invariant comparison. We adopt the 3D generative model metrics as follows:

- **Fidelity** (NN-CD, lower is better) measures the mean Chamfer Distance in Eq. (8) from each generated mesh to its nearest training mesh, quantifying how closely generated shapes resemble real specimens.

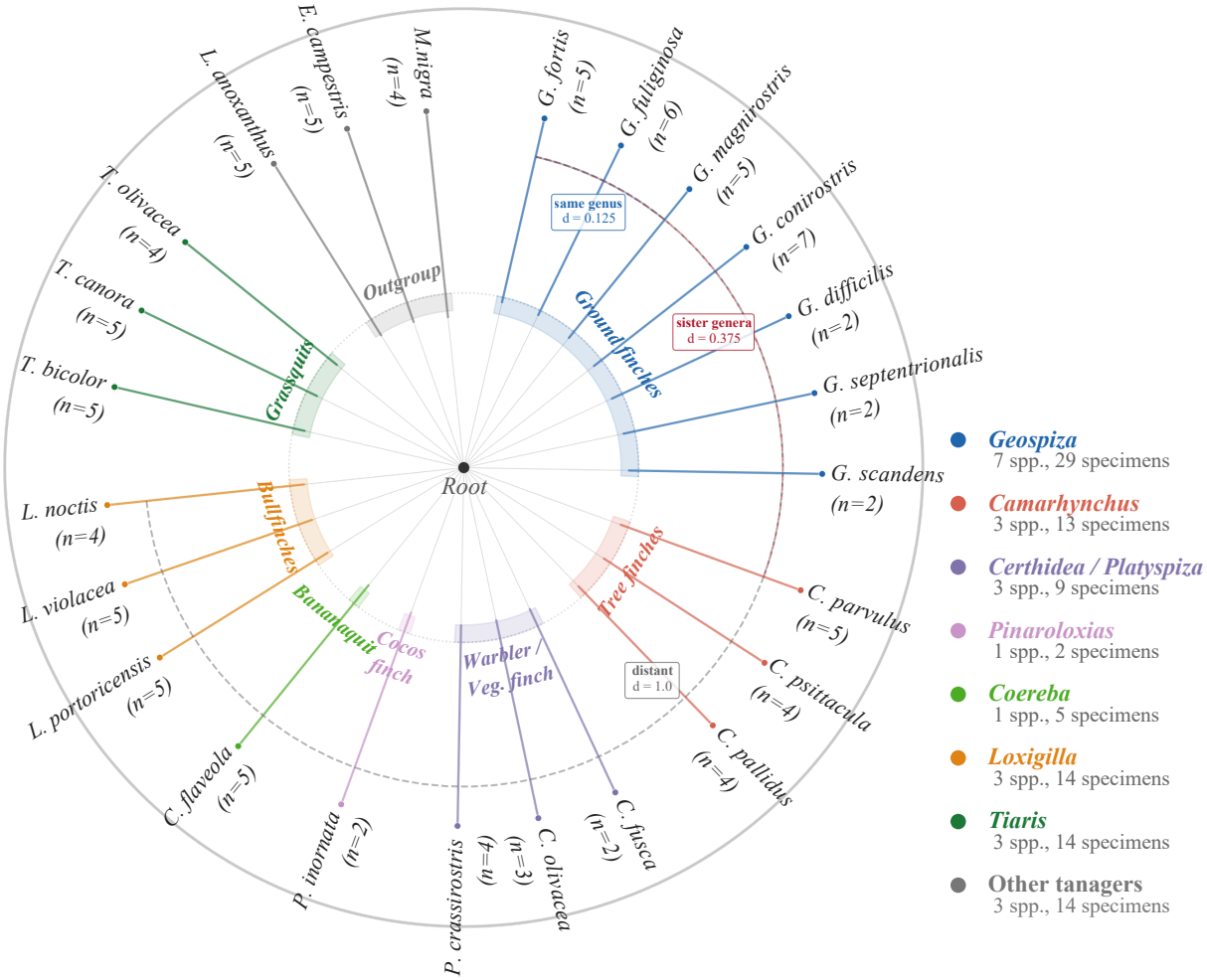

Figure 4: **Phylogenetic tree and dataset composition for the 24 species and $N = 100$ specimens used in all experiments.** Species are organized into eight biologically defined clades: *Geospiza* (ground finches, 7 species, 29 specimens), *Camarhynchus* (tree finches, 3 species, 13 specimens), *Certhidea/Platyspiza* (warbler and vegetarian finches, 3 species, 9 specimens), *Pinaroloxias* (Cocos finch, 1 species, 2 specimens), *Coereba* (bananaquit, 1 species, 5 specimens), *Loxigilla* (bullfinches, 3 species, 14 specimens), *Tiaris* (grassquits, 3 species, 14 specimens), and outgroup tanagers (3 species, 14 specimens). Normalized pairwise phylogenetic distances d_{phylo} are assigned at several levels, such as congeneric species pairs ($d = 0.125$), sister genera ($d = 0.375$), and all remaining pairs ($d = 1.0$), following the genus-level taxonomy of Darwin's Finches and their relatives.

- **Diversity** (Pairwise CD, higher is better) is the mean pairwise Chamfer Distance among generated meshes, capturing whether the model produces varied outputs or collapses to a single mode.
- **Coverage** (COV, higher is better) reports the fraction of training shapes that have at least one generated neighbor within a distance threshold, measuring how well the generated distribution spans the training distribution.
- **Minimum Matching Distance** (MMD, lower is better) provides a complementary distributional distance by computing the average distance from each training mesh to its closest generated counterpart.
- **Intra-species diversity**, defined as the pairwise CD among species-conditioned generated samples expressed as a percentage of the corresponding real intra-species CD. This metric directly measures

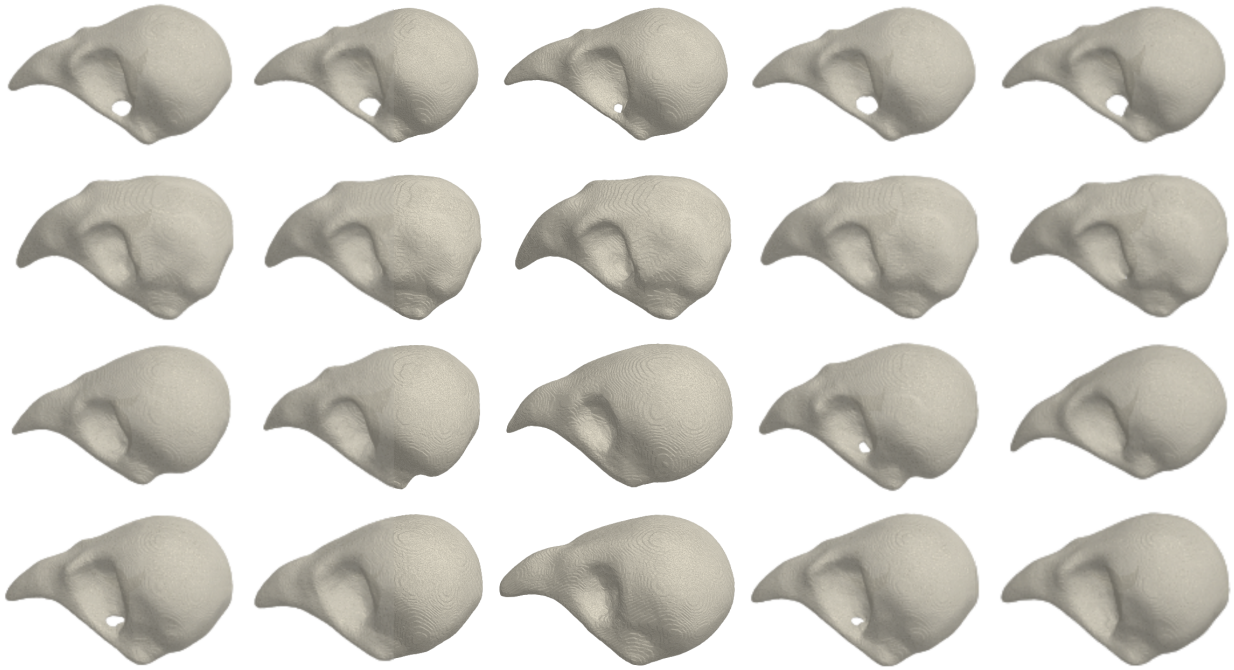

Figure 5: **Species-conditioned skull meshes generated by Residual CFM for the four focal species.** Each row shows five independently sampled outputs from the same species conditioning. Row 1 (*G. fortis*): compact skulls with short, deep beaks characteristic of a seed-cracking ground finch. Row 2 (*G. magnirostris*): larger cranial vaults and broader beaks consistent with this species' role as the large ground finch. Row 3 (*G. fuliginosa*): smaller overall skull size with narrower beak proportions. Row 4 (*C. parvulus*): rounder cranial profile with a finer, more pointed beak reflecting the tree finch body plan. Within-row variation confirms that the model does not collapse to a single mode; between-row differences confirm species-appropriate conditioning. All meshes are decoded at 256^3 resolution via Marching Cubes and rendered in lateral view.

whether the model captures the biologically relevant within-species variation rather than merely producing between-species diversity.

- **Latent Phylogenetic Consistency** (LPC) is the Pearson correlation between inter-species latent and phylogenetic distances, quantifying how faithfully the learned representation reflects evolutionary relationships.
- **Morphometric Fréchet Distance** (Morph. FID, lower is better) computes a Fréchet distance on a 12-dimensional vector of morphometric shape descriptors (surface area, volume, bounding box dimensions, elongation, flatness, compactness, vertex count, and centroid position), providing a biologically-grounded distributional quality metric analogous to FID.

We additionally introduce three generativity verification tests specifically designed for the small-data regime (see Section 5.5).

5.4 Main Results

Figure 5 shows five representative generated skulls per species, demonstrating that the Residual CFM produces morphologically distinct and species-appropriate outputs across all four focal taxa.

SI Fig. S1 compares the within-species diversity of Residual CFM and GMM samples for *G. fuliginosa*. Table 1 presents the primary quantitative comparison across all methods. All reported numbers are from the final experimental run producing 360 meshes (180 via Residual CFM and 180 via GMM), with each method generating 100 unconditional samples and 10 species-conditioned samples for each of four focal species (*G. fortis*, *G. magnirostris*, *G. fuliginosa*, *C. parvulus*) as well as 20 ancestral reconstructions for each of two species pairs.

Method	Fidelity↓	Diversity↑	COV↑	MMD↓	LPC↑	Morph. FD↓	Intra-sp.
DDPM	—	—	—	—	—	—	0%
Standard CFM	0.00197	0.00595	—	—	0.993	—	3–6%
GMM†	0.00190	0.00766	—	—	—	13,322	28–50%
Res. CFM (ours)	**0.00181**	**0.00755**	**0.53**	**9.77**	**0.993**	**10,641**	**88–129%**
Training ref.	—	0.01376	1.00	—	—	—	100%

Table 1: **Main quantitative results.** Best neural method in **bold**. †Non-neural baseline. DDPM produced no valid meshes.

		Mesh-level CD (%)		Code-level ratio	
Species	n	**Res. CFM**	**GMM**	**Res. CFM**	**GMM**
G. fortis	5	5.2%	27.6%	0.96×	1.14×
G. magnirostris	5	6.5%	34.7%	0.88×	1.13×
G. fuliginosa	6	42.3%	32.2%	1.29×	1.36×
C. parvulus	5	15.3%	49.7%	1.19×	1.12×

Table 2: Per-species diversity (mesh-level pairwise Chamfer distance (CD) as % of training diversity) and code-level variation ratio (generated std / real std).

DDPM with 1,000 denoising steps produced catastrophically unstable outputs. During training, the standard deviation of generated codes oscillated wildly, between 0.17× and 338× the true value across epochs, and the model never converged to a stable generative regime. No valid 3D meshes could be extracted from any generated code. This failure is consistent with the theoretical expectation that iterative Markov chains require per-step accuracy that is unattainable with only 1,107 training points in 64 dimensions. As approximation errors at each of the 1,000 steps compound multiplicatively, pushing generated codes far outside the data manifold. This result carries a practical implication for the field: DDPM and related multi-step diffusion models should not be applied to small scientific datasets without fundamental architectural modifications.

Standard conditional flow matching converged to a stable model but exhibited severe mode collapse, producing only 3–6% of real intra-species variation (see SI Fig. S2). Importantly, the model learned the correct between-species structure (species centroids were accurately placed in latent space, as evidenced by the high LPC of 0.993), but entirely failed to capture within-species variation. This is precisely the failure mode predicted by our analysis in Stage 3: Residual Conditional Flow Matching with ∼4 training points per conditioned class, the MSE-optimal velocity field converges to the conditional mean. The standard CFM result thus serves as a controlled ablation that isolates the contribution of our residual decomposition.

The proposed Residual CFM overcomes both failure modes by factorizing generation into analytic centroid lookup and neural residual prediction. At the code level, it achieves 88–129% of real intra-species variation across the four focal species, variation that is genuinely generated, not memorized, as verified by our three-test framework (see Section 5.5). Compared to the GMM baseline, Residual CFM achieves superior fidelity (0.00181 vs. 0.00190) and a 20% lower morphometric Fréchet distance (10,641 vs. 13,322), indicating closer distributional matching in biologically meaningful feature space.

Table 2 provides a per-species breakdown of both mesh-level and code-level diversity for the four focal species. The discrepancy between code-level diversity (88–129%) and mesh-level Chamfer distance (CD) diversity (5–42%) reflects the non-linear decoder: small code perturbations near species centroids produce visually distinct but geometrically similar meshes. The code-level metric captures the full variation learned by the generative model; the mesh-level metric is more conservative and influenced by the SDF decoder's smoothing effect.

In unconditional generation mode, the Residual CFM spans 72.7% of training diversity, compared to GMM's 60.8%, confirming broader morphospace coverage. These results establish the Residual CFM as the first neural generative model to successfully produce diverse, species-appropriate 3D biological morphology from a dataset of only 100 specimens.

Test	Metric	Value
1. Memorization	Memorized meshes	0 / 180
2. Residual signal	$\|\mathbf{r}\| \,/\, \|\boldsymbol{\mu}_a - \boldsymbol{\mu}_b\|$	42.0% (>15%)
3. Mesh novelty	Gen-NN / Same-sp	26.4% (in 20–80%)

Table 3: **Generativity verification.** All three independent tests confirm genuine generation.

Configuration	Training codes	Phylo loss	Diversity ratio
A: Baseline	100	×	3,039
B: + Augmentation	1,107	×	1,198
C: + Phylo only	100	✓	3,105
D: Full model	1,107	✓	**877**

Table 4: **Ablation.** Diversity ratio = mean pairwise distance (generated) / (real). Closer to 1.0 is better.

5.5 Generativity Verification

A critical concern for any generative model trained on a small dataset is whether the model genuinely generates novel shapes or merely memorizes, interpolates, or trivially perturbs the training data. Standard generative model evaluation metrics (e.g., FID) assume large reference sets and lose discriminative power when $N = 100$. We therefore propose a generativity verification framework consisting of three independent tests (memorization check, residual meaningfulness, and mesh-level novelty) specifically designed for validating generative models on small scientific datasets where conventional metrics are unreliable.

5.5.1 Test 1: Memorization Check

For each of the 180 CFM-generated meshes, we compute its Chamfer Distance to all 100 training meshes after normalizing both to the unit cube. A generated mesh is flagged as "memorized" if its distance to the nearest training mesh falls below 10% of the minimum same-species training distance, yielding a threshold of 0.000038. Of 180 generated meshes, zero fall below this threshold, confirming that the model does not reproduce training examples.

5.5.2 Test 2: Residual Meaningfulness

This test asks whether the learned residuals carry genuine morphological information or are negligibly small (which would indicate that the model is effectively a centroid-lookup table). We compute the mean residual magnitude $\mathbb{E}[\|\mathbf{r}_i\|_2] = 0.380$ and compare it to the mean inter-species centroid distance $\mathbb{E}[\|\boldsymbol{\mu}_a - \boldsymbol{\mu}_b\|_2] = 0.904$. The resulting ratio of 42.0% far exceeds the 15% threshold below which residuals would be considered negligible, confirming that the flow model captures substantial within-species morphological variation beyond what the centroid alone provides.

5.5.3 Test 3: Mesh-level Novelty Ratio

The most stringent test directly examines mesh geometry. We define the novelty ratio $\rho = \mathrm{CD}_{\text{gen-to-nearest}}/\mathrm{CD}_{\text{same-species}}$, where the numerator is the mean Chamfer Distance from each generated mesh to its nearest training mesh and the denominator is the mean pairwise CD among real same-species specimens. If $\rho < 10\%$, generated meshes are essentially copies of training data; if $\rho \in [20\%, 80\%]$, they exhibit genuine novel variation within the biological range; if $\rho > 100\%$, the model generates more variation than real biology. We obtain $\rho = 26.4\%$, squarely in the genuine-generation range. Together, these three tests provide converging evidence that the Residual CFM produces shapes that are neither memorized nor trivially derived from the training set. Table 3 summarizes our three generative tests.

5.6 Ablation Study

To disentangle the contributions of our two key ingredients, latent augmentation and phylogenetic consistency loss. We train four configurations of the Conditional diffusion model (DDPM, 500 timesteps, cosine schedule) on the full latent codes and measure the diversity ratio (mean pairwise distance of generated codes divided by that of real codes, and a value of 1.0 indicates perfect diversity matching). Table 4 reports the results.

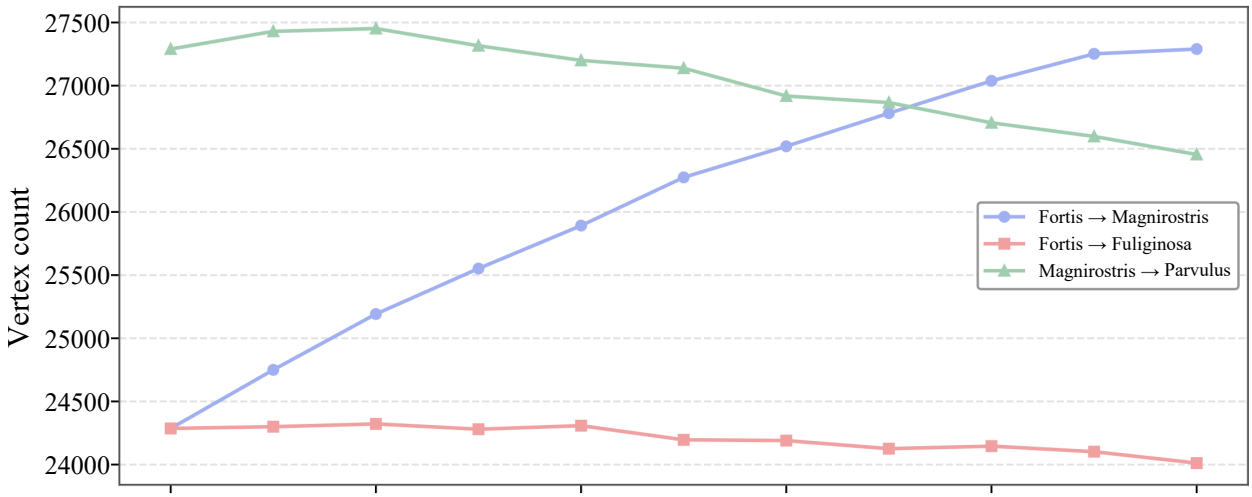

Figure 6: **Latent interpolation smoothness.** Vertex counts (a proxy for skull size) change monotonically along interpolation paths between species centroids, confirming a smooth, well-structured latent space.

The baseline configuration (Config A), which trains the diffusion model on only the 100 original codes without phylogenetic loss, achieves a diversity ratio of 3,039, indicating that generated codes are clustered far too tightly relative to the real distribution. Adding augmentation alone (Config B) reduces the ratio to 1,198, a 61% improvement, confirming that the augmented training set provides the sample volume needed for the flow model to learn a broader residual distribution. Adding phylogenetic loss alone without augmentation (Config C) yields a ratio of 3,105, essentially unchanged from the baseline; this demonstrates that phylogenetic regularization cannot compensate for the fundamental sample-size deficiency. The full model (Config D) combines both ingredients to achieve a ratio of 877, a 27% further improvement over augmentation alone. This analysis reveals a clear decomposition of roles: augmentation addresses the sample-size bottleneck by providing enough training codes for the generative model to learn a non-degenerate distribution, while phylogenetic loss addresses the structural bottleneck by organizing the latent space for more coherent generation. Although this ablation uses a diffusion baseline rather than the Residual CFM employed in our final pipeline, it isolates the effects of augmentation and phylogenetic regularization on the shared latent space from which all methods generate.

5.7 Reconstruction Quality

To validate that Stage 1 faithfully encodes training shapes, we decode each learned latent code back to a mesh and measure the Chamfer Distance (CD) to the original specimen. Over all 100 specimens, reconstruction succeeded for 100/100 meshes with mean CD = 0.0022, median CD = 0.0004, and maximum CD = 0.0112. The low median confirms that the vast majority of specimens are represented with high fidelity; the few higher-CD cases correspond to specimens with complex thin structures.

5.8 Interpolation Smoothness

To demonstrate that the latent space supports smooth morphological transitions, we generate interpolation sequences between species pairs by computing $\mathbf{z}_t = (1-t)\boldsymbol{\mu}_a + t\boldsymbol{\mu}_b$ for $t \in \{0, 0.1, \ldots, 1.0\}$ and decoding each to a mesh.

Figure 6 shows that vertex counts and mesh change monotonically and smoothly: *G. fortis*→*G. magnirostris* transitions smoothly from 24,286 to 27,290 vertices (reflecting increasing skull size), while *G. fortis*→*G. fuliginosa* shows a gentle decrease from 24,286 to 24,012. The Chamfer Distance to endpoints changes monotonically along the path, confirming the absence of discontinuities or mode switching.

5.9 Leave-One-Species-Out Generalization

A key property of a phylogenetically-structured latent space is that it should support generation for species entirely absent from training, using evolutionary relationships to infer a plausible location in morphospace.

We test this with a leave-one-species-out (LOSO) protocol across all 18 species with ≥ 4 specimens. For each held-out species, its latent centroid is estimated as an inverse-distance-weighted mean of the three phylogenetically nearest training species, and new shapes are generated by sampling residuals from the global residual distribution conditioned on this predicted centroid. No model retraining occurs; the experiment tests latent space geometry alone.

The centroid prediction error averages 0.36 across species, against a mean within-species spread of 0.62 (see SI Fig. S3), meaning the predicted centroid lands well within the cloud of real intra-species variation for most species. The ratio of generated-to-nearest-real Chamfer distance to within-species Chamfer distance averages 1.25×, indicating that generated shapes are moderately less faithful than real intra-species variation. Given that the model has never observed any specimen from the held-out species, a ratio close to 1.0 is not expected; 1.25× represents a practically useful approximation of unseen morphology.

Performance varies systematically with phylogenetic isolation. Well-embedded species (*C. psittacula*, 1.12×; *G. fortis*, 1.13×) are surrounded by closely related training species and benefit from accurate centroid interpolation. The worst-performing species (*P. crassirostris*, 1.46×) is phylogenetically isolated. Its nearest neighbors are substantially more distant than for any Geospiza species, and the centroid estimate is correspondingly less reliable. This systematic pattern is consistent with the hypothesis that $\mathcal{L}_{\text{phylo}}$ has structured the latent space along evolutionary lines, though we note that the distance proxy may underestimate true phylogenetic isolation for species like *P. crassirostris*, and that results for species with only 4 specimens should be interpreted cautiously (see SI Section S2 and Table S3 for the complete LOSO results).

5.10 Morphometric Fréchet Distance

Standard image-based FID [17] is not applicable to 3D meshes, as it relies on Inception network activations trained on ImageNet. We introduce **MorphFID**, a Fréchet distance computed in the space of biologically interpretable morphometric descriptors rather than learned image features. Each mesh is represented by a 12-dimensional feature vector comprising surface area, volume, three bounding box extents, elongation, flatness, compactness, vertex count, and three centroid coordinates. Features are z-scored using training set statistics, and the Fréchet distance between two sets of shapes is computed as the standard matrix form (Eq. (7)) applied to the resulting 12-dimensional Gaussian fits. This metric directly measures whether the generated distribution matches the training distribution in the morphological properties most relevant to biological shape analysis.

Residual CFM achieves a MorphFID of **10,641**, compared to GMM's **13,322**, which is a 20% reduction, indicating that CFM-generated shapes more faithfully approximate the training distribution in morphometric feature space. Lower MorphFID reflects better coverage of the observed range of skull sizes, proportions, and compactness values. The absolute values are not directly comparable across datasets; what is meaningful is the relative improvement of CFM over GMM, and the direction of the gap is consistent with the method comparison results in Section 5. All evaluation metrics for the final Residual CFM model are consolidated in SI Table S4.

5.11 Ancestral Reconstruction

We reconstruct hypothetical common ancestors by interpolating species centroids and phylogenetic embeddings (Eq. (17)). For the interpolation between *G. fortis* and *G. magnirostris*, the ancestor meshes have vertex counts intermediate between the two species. For the interpolation between *G. fortis* and *G. fuliginosa*, the ancestor is closest to *G. fuliginosa* (CD ≈ 0.0008), consistent with their closer phylogenetic relationship. These results demonstrate that the phylogenetically structured latent space enables biologically meaningful ancestral inference. Figure 7 demonstrates several examples of latent space interpolation.

6 Discussion

6.1 Why Residual Decomposition Works

The central methodological insight of this work is that the group structure inherent in biological data, that is, species labels, can be exploited to dramatically simplify the generative modeling task. By decomposing each latent code into a species centroid and a residual, we separate the problem into two components of fundamentally different character. The centroid captures where each species resides in morphospace; this is a discrete lookup operation that requires no learning and can be computed analytically from the training

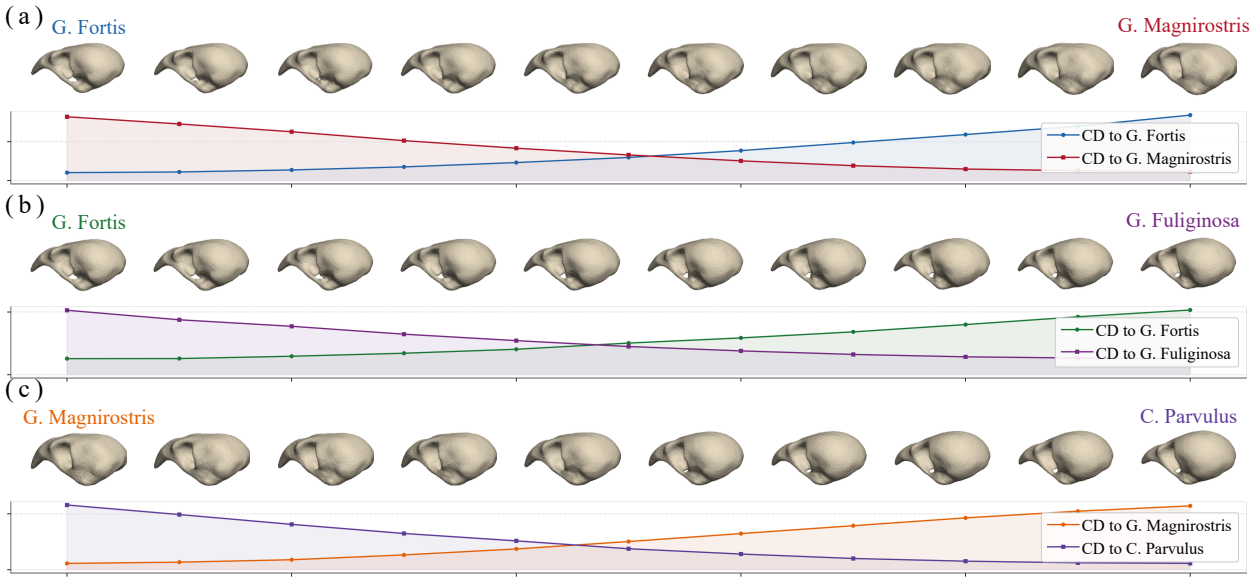

Figure 7: **Latent space interpolation between three species pairs, each showing 11 uniformly spaced steps from the source centroid (left) to the target centroid (right).** (a) From *G. fortis* to *G. magnirostris* (congeneric, $d_{\text{phylo}} = 0.125$); beak depth increases monotonically, and cranial vault enlarges progressively. (b) From *G. fortis* to *G. fuliginosa* (congeneric, $d_{\text{phylo}} = 0.125$); overall skull size decreases while beak proportions narrow continuously. (c) From *G. magnirostris* to *C. parvulus* (sister genera, $d_{\text{phylo}} = 0.375$); a more pronounced shape transition.

data. The residual captures how individual specimens vary around their species mean; crucially, because all residuals are zero-centered regardless of species identity, they can be pooled into a single shared distribution of 100 examples rather than 24 separate distributions of ∼4 examples each.

This increase in effective sample size is the primary mechanism that makes neural generation feasible at this data scale. The principle is general: it applies to any setting in which data is organized into labeled groups with limited per-group samples, e.g., organ morphology across patient subgroups, cell shapes across genetic backgrounds, or material microstructures across alloy compositions.

6.2 Role of Phylogenetic Consistency Loss

While the residual decomposition addresses the sample-size bottleneck, the phylogenetic consistency loss addresses a complementary structural bottleneck. Without this regularization, the DeepSDF latent space is organized purely by reconstruction fidelity, and there is no guarantee that the resulting code geometry reflects evolutionary relationships. Our loss (Eq. (9)) explicitly encourages pairwise latent distances to track phylogenetic distances, grounding the representation in established evolutionary theory. The ablation study (Section 5.6) confirms that phylogenetic loss alone does not solve the diversity problem (Config C: ratio 3,105 vs. baseline 3,039), but when combined with augmentation, it provides a meaningful further improvement (Config D: ratio 877 vs. Config B: 1,198, a 27% reduction).

More importantly, the phylogenetically-structured latent space is what enables two of our most biologically interesting applications: ancestral morphology reconstruction via centroid interpolation, and leave-one-species-out prediction via phylogenetic neighbor weighting.

6.3 Neural vs. Statistical Generation

The GMM baseline achieves respectable per-species diversity (28–50%) without any learned generative model, raising a natural question: When is a neural approach preferable? Our answer is twofold. First, the Residual CFM achieves better fidelity (0.00181 vs. 0.00190) and a substantially lower morphometric Fréchet distance (10,641 vs. 13,322), indicating more faithful distribution matching. Second, the GMM assumes that within-species variation is Gaussian, which becomes increasingly limiting as datasets grow or for species with

complex, multimodal variation patterns such as sexual dimorphism [41] or seasonal polymorphism. The neural model provides a scalable foundation that can absorb additional complexity as larger morphological datasets become available.

6.4 Limitations

Several limitations of the current work merit discussion. The phylogenetic distance proxy relies on branch lengths from molecular phylogenies, which may not perfectly reflect morphological divergence rates, particularly for lineages that have undergone rapid adaptive radiation or convergent evolution. Also, using a continuous patristic distance matrix derived from molecular phylogeny [42] might be more precise. The coverage score of 0.53 indicates that the model does not yet span the full training distribution, suggesting room for improvement in the augmentation or flow-matching components. Furthermore, the leave-one-species-out experiment uses the same DeepSDF decoder trained on all species; a fully held-out protocol would require retraining the decoder from scratch for each fold, which is computationally prohibitive but would provide a stricter test of generalization. Finally, and perhaps most importantly, the biological plausibility of generated specimens ultimately requires expert morphological evaluation by comparative anatomists, which we leave to future collaborative work.

6.5 Broader Impact

PhyloSDF opens several avenues for computational evolutionary biology. By enabling virtual specimen augmentation, the model can supplement small morphological datasets for statistical analyses that currently suffer from low statistical power, potentially reducing the need for destructive sampling of rare or irreplaceable museum material. The ancestral reconstruction capability provides a data-driven complement to existing phylogenetic comparative methods, allowing researchers to generate and visualize hypothetical ancestral morphologies as full 3D meshes rather than abstract trait vectors. More broadly, the residual decomposition framework demonstrates that neural generative models can be made to function in scientific data regimes far smaller than typically assumed, which may encourage adoption of these methods across the biological sciences. We emphasize that generated specimens should be clearly labeled as synthetic in any downstream analysis, and that expert morphological evaluation remains essential for validating biological plausibility.

7 Conclusion

We have presented PhyloSDF, the first neural generative model for phylogenetically structured 3D biological morphology. The key architectural contribution of this work is Residual Conditional Flow Matching, which transforms an intractable small-data generation problem into a tractable one by factorizing the task into analytic species-centroid lookup and learned residual prediction. This decomposition increases the effective training set from $\sim$4 specimens per species to 100 pooled residuals, enabling a lightweight 283K-parameter flow model to capture genuine intra-species morphological variation. Combined with our phylogenetic consistency loss, which structures the latent space to reflect evolutionary distances, and targeted latent augmentation strategies, the model generates novel, species-appropriate finch skull meshes that pass all three of our proposed generativity verification tests: zero memorization among 180 generated meshes, 42% residual meaningfulness, and 26.4% mesh-level novelty ratio.

The experimental results demonstrate that the Residual CFM outperforms both denoising diffusion (which fails entirely at this data scale) and standard flow matching (which mode-collapses), while achieving better fidelity and distributional matching than a Gaussian mixture baseline. Leave-one-species-out experiments across 18 species and smooth latent interpolations further confirm the biological utility of the phylogenetically-structured representation.

Looking forward, several directions merit investigation. Scaling to larger morphological datasets (hundreds to thousands of specimens) would allow testing whether the residual framework continues to outperform direct generation as data grows. Incorporating additional biological priors, such as allometric scaling laws or developmental constraints, into the loss function could further improve biological plausibility. Extending the framework to articulated or deformable structures (e.g., full skeletal assemblages or soft-tissue organs) would broaden its applicability. We hope this work establishes generative modeling as a practical and rigorous tool for evolutionary biology, enabling computational morphologists to synthesize, explore, and test hypotheses about biological form.

References

[1] J. A. Cunningham, I. A. Rahman, S. Lautenschlager, E. J. Rayfield, and P. C. Donoghue, "A virtual world of paleontology," *Trends in Ecology & Evolution*, vol. 29, no. 6, pp. 347–357, 2014.

[2] T. G. Davies, I. A. Rahman, S. Lautenschlager, J. A. Cunningham, R. J. Asher, P. M. Barrett, K. T. Bates, S. Bengtson, R. B. J. Benson, D. M. Boyer, J. Braga, J. A. Bright, L. P. A. M. Claessens, P. G. Cox, X.-P. Dong, A. R. Evans, P. L. Falkingham, M. Friedman, R. J. Garwood, A. Goswami, J. R. Hutchinson, N. S. Jeffery, Z. Johanson, R. Lebrun, C. Martínez-Pérez, J. Marugán-Lobón, P. M. O'Higgins, B. Metscher, M. Orliac, T. B. Rowe, M. Rücklin, M. R. Sánchez-Villagra, N. H. Shubin, S. Y. Smith, J. M. Starck, C. Stringer, A. P. Summers, M. D. Sutton, S. A. Walsh, V. Weisbecker, L. M. Witmer, S. Wroe, Z. Yin, E. J. Rayfield, and P. C. J. Donoghue, "Open data and digital morphology," *Proceedings of the Royal Society B: Biological Sciences*, vol. 284, no. 1852, p. 20170194, 2017.

[3] C. P. Klingenberg, "Evolution and development of shape: integrating quantitative approaches," *Nature Reviews Genetics*, vol. 11, no. 9, pp. 623–635, 2010.

[4] K. Keklikoglou, S. Faulwetter, E. Chatzinikolaou, P. Wils, J. Brecko, J. Kvaček, B. Metscher, and C. Arvanitidis, "Micro-computed tomography for natural history specimens: a handbook of best practice protocols," *European Journal of Taxonomy*, no. 522, pp. 1–55, 2019.

[5] C. Bardua, R. N. Felice, A. Watanabe, A. C. Fabre, and A. Goswami, "A practical guide to sliding and surface semilandmarks in morphometric analyses," *Integrative Organismal Biology*, vol. 1, no. 1, pp. 1–34, 2019.

[6] J. M. Mulqueeney, A. Searle-Barnes, A. Brombacher, M. Sweeney, A. Goswami, and T. H. G. Ezard, "How many specimens make a sufficient training set for automated three-dimensional feature extraction?," *Royal Society Open Science*, vol. 11, no. 6, p. rsos.240113, 2024.

[7] D. P. Kingma and M. Welling, "Auto-encoding variational Bayes," *arXiv preprint arXiv:1312.6114*, 2013.

[8] I. Goodfellow, J. Pouget-Abadie, M. Mirza, B. Xu, D. Warde-Farley, S. Ozair, A. Courville, and Y. Bengio, "Generative adversarial networks," *Communications of the ACM*, vol. 63, no. 11, pp. 139–144, 2020.

[9] J. Ho, A. Jain, and P. Abbeel, "Denoising diffusion probabilistic models," *Advances in Neural Information Processing Systems*, vol. 33, pp. 6840–6851, 2020.

[10] Y. Lipman, R. T. Chen, H. Ben-Hamu, M. Nickel, and M. Le, "Flow matching for generative modeling," in *11th International Conference on Learning Representations (ICLR 2023)*, 2023.

[11] G. van den Burg and C. Williams, "On memorization in probabilistic deep generative models," *Advances in Neural Information Processing Systems*, vol. 34, pp. 27916–27928, 2021.

[12] C. Zhang, S. Bengio, M. Hardt, B. Recht, and O. Vinyals, "Understanding deep learning (still) requires rethinking generalization," *Communications of the ACM*, vol. 64, no. 3, pp. 107–115, 2021.

[13] J. Felsenstein, "Phylogenies and the comparative method," *The American Naturalist*, vol. 125, no. 1, pp. 1–15, 1985.

[14] J. Lucas, G. Tucker, R. Grosse, and M. Norouzi, "Understanding posterior collapse in generative latent variable models," in *ICLR 2019 Workshop DeepGenStruct*, 2019.

[15] M. J. Chong and D. Forsyth, "Effectively unbiased FID and inception score and where to find them," in *2020 IEEE/CVF Conference on Computer Vision and Pattern Recognition (CVPR)*, pp. 6069–6078, 2020.

[16] J. J. Park, P. Florence, J. Straub, R. Newcombe, and S. Lovegrove, "DeepSDF: Learning continuous signed distance functions for shape representation," in *2019 IEEE/CVF Conference on Computer Vision and Pattern Recognition (CVPR)*, pp. 165–174, 2019.

[17] M. Heusel, H. Ramsauer, T. Unterthiner, B. Nessler, and S. Hochreiter, "GANs trained by a two time-scale update rule converge to a local Nash equilibrium," *Advances in Neural Information Processing Systems*, vol. 30, 2017.

[18] L. Mescheder, M. Oechsle, M. Niemeyer, S. Nowozin, and A. Geiger, "Occupancy networks: Learning 3D reconstruction in function space," in *2019 IEEE/CVF Conference on Computer Vision and Pattern Recognition (CVPR)*, pp. 4455–4465, 2019.

[19] Z. Chen and H. Zhang, "Learning implicit fields for generative shape modeling," in *2019 IEEE/CVF Conference on Computer Vision and Pattern Recognition (CVPR)*, (Los Alamitos, CA, USA), pp. 5932–5941, IEEE Computer Society, June 2019.

[20] J. Chibane, A. Mir, and G. Pons-Moll, "Neural unsigned distance fields for implicit function learning," in *Proceedings of the 34th International Conference on Neural Information Processing Systems*, (Red Hook, NY, USA), pp. 21638–21652, Curran Associates Inc., 2020.

[21] M. Niemeyer, L. Mescheder, M. Oechsle, and A. Geiger, "Differentiable volumetric rendering: Learning implicit 3D representations without 3D supervision," in *2020 IEEE/CVF Conference on Computer Vision and Pattern Recognition (CVPR)*, pp. 3501–3512, 2020.

[22] P. Achlioptas, O. Diamanti, I. Mitliagkas, and L. Guibas, "Learning representations and generative models for 3D point clouds," in *International Conference on Machine Learning*, pp. 40–49, PMLR, 2018.

[23] G. Yang, X. Huang, Z. Hao, M.-Y. Liu, S. Belongie, and B. Hariharan, "PointFlow: 3D point cloud generation with continuous normalizing flows," in *2019 IEEE/CVF International Conference on Computer Vision (ICCV)*, pp. 4540–4549, 2019.

[24] D. Maturana and S. Scherer, "VoxNet: A 3D convolutional neural network for real-time object recognition," in *2015 IEEE/RSJ International Conference on Intelligent Robots and Systems (IROS)*, pp. 922–928, 2015.

[25] C. Nash, Y. Ganin, S. M. A. Eslami, and P. Battaglia, "PolyGen: An autoregressive generative model of 3D meshes," in *Proceedings of the 37th International Conference on Machine Learning* (H. D. III and A. Singh, eds.), vol. 119 of *Proceedings of Machine Learning Research*, pp. 7220–7229, PMLR, 2020.

[26] Z. Hao, H. Averbuch-Elor, N. Snavely, and S. Belongie, "DualSDF: Semantic shape manipulation using a two-level representation," in *2020 IEEE/CVF Conference on Computer Vision and Pattern Recognition (CVPR)*, p. 7628–7638, IEEE, 2020.

[27] A. Vahdat, F. Williams, Z. Gojcic, O. Litany, S. Fidler, K. Kreis, *et al.*, "LION: Latent point diffusion models for 3D shape generation," *Advances in Neural Information Processing Systems*, vol. 35, pp. 10021–10039, 2022.

[28] K. Bartoszek, "The phylogenetic effective sample size and jumps," *Mathematica Applicanda*, vol. 46, July 2018.

[29] C. O. Webb, D. D. Ackerly, M. A. McPeek, and M. J. Donoghue, "Phylogenies and community ecology," *Annual Review of Ecology and Systematics*, vol. 33, no. 1, pp. 475–505, 2002.

[30] M. Pagel, "Inferring the historical patterns of biological evolution," *Nature*, vol. 401, no. 6756, pp. 877–884, 1999.

[31] A. Gropp, L. Yariv, N. Haim, M. Atzmon, and Y. Lipman, "Implicit geometric regularization for learning shapes," in *Proceedings of the 37th International Conference on Machine Learning (ICML)*, pp. 3789–3799, 2020.

[32] S. Osher and R. Fedkiw, *Level Set Methods and Dynamic Implicit Surfaces*, vol. 153. Springer Science & Business Media, 2002.

[33] K. J. Burns, A. J. Shultz, P. O. Title, N. A. Mason, F. K. Barker, J. Klicka, S. M. Lanyon, and I. J. Lovette, "Phylogenetics and diversification of tanagers (Passeriformes: Thraupidae), the largest radiation of Neotropical songbirds," *Molecular Phylogenetics and Evolution*, vol. 75, pp. 41–77, 2014.

[34] K. J. Burns, S. J. Hackett, and N. K. Klein, "Phylogenetic relationships and morphological diversity in Darwin's finches and their relatives," *Evolution*, vol. 56, no. 6, pp. 1240–1252, 2002.

[35] M. S. Albergo and E. Vanden-Eijnden, "Building normalizing flows with stochastic interpolants," in *International Conference on Learning Representations (ICLR)*, 2023.

[36] A. Tong, K. Fatras, N. Malkin, G. Huguet, Y. Zhang, J. Rector-Brooks, G. Wolf, and Y. Bengio, "Improving and generalizing flow-based generative models with minibatch optimal transport," *Transactions on Machine Learning Research*, pp. 1–34, 2024.

[37] D. C. Dowson and B. V. Landau, "The Fréchet distance between multivariate normal distributions," *Journal of Multivariate Analysis*, vol. 12, no. 3, pp. 450–455, 1982.

[38] M. Tokita, W. Yano, H. F. James, and A. Abzhanov, "Cranial shape evolution in adaptive radiations of birds: comparative morphometrics of Darwin's finches and Hawaiian honeycreepers," *Philosophical Transactions of the Royal Society B: Biological Sciences*, vol. 372, no. 1713, p. 20150481, 2017.

[39] S. Al-Mosleh, G. P. T. Choi, A. Abzhanov, and L. Mahadevan, "Geometry and dynamics link form, function, and evolution of finch beaks," *Proceedings of the National Academy of Sciences*, vol. 118, no. 46, p. e2105957118, 2021.

[40] S. Mosleh, G. P. T. Choi, G. M. Musser, H. F. James, A. Abzhanov, and L. Mahadevan, "Beak morphometry and morphogenesis across avian radiations," *Proceedings of the Royal Society B: Biological Sciences*, vol. 290, no. 2007, p. 20230420, 2023.

[41] D. W. Frayer and M. H. Wolpoff, "Sexual dimorphism," *Annual Review of Anthropology*, vol. 14, pp. 429–473, 1985.

[42] T. N. Lamichhane, R. S. Raiker, and S. M. Jay, "Exogenous dna loading into extracellular vesicles via electroporation is size-dependent and enables limited gene delivery," *Molecular Pharmaceutics*, vol. 12, no. 10, p. 3650–3657, 2015.

[43] D. P. Kingma and J. Ba, "Adam: A method for stochastic optimization," in *International Conference on Learning Representations (ICLR)*, 2015.

[44] P. Zhou, X. Xie, Z. Lin, and S. Yan, "Towards understanding convergence and generalization of AdamW," *IEEE Transactions on Pattern Analysis and Machine Intelligence*, vol. 46, no. 9, pp. 6486–6493, 2024.

[45] X. Ma, C. Qin, H. You, H. Ran, and Y. Fu, "Rethinking network design and local geometry in point cloud: A simple residual MLP framework," in *International Conference on Learning Representations (ICLR)*, 2022.

[46] D. Hendrycks and K. Gimpel, "Gaussian error linear units (GELUs)," *arXiv preprint arXiv:1606.08415*, 2016.

Supplementary Information

S1 Algorithm and Implementation Details

Algorithm 1 summarizes the procedure of our Residual CFM Generation algorithm.

Algorithm 1 Residual CFM Generation

Require: Species s, phylo embedding ϕ_s, centroid $\boldsymbol{\mu}_s$, velocity network $\mathbf{v}_\theta$, normalization stats $(\mu_\mathbf{r}, \sigma_\mathbf{r})$, Euler steps $K = 50$

$\mathbf{x}_0 \sim \mathcal{N}(\mathbf{0}, \mathbf{I}_{64})$
$dt \leftarrow 1/K$
for $k = 0, \ldots, K-1$ **do**
  $t \leftarrow k \cdot dt$
  $\mathbf{v} \leftarrow \mathbf{v}_\theta(\mathbf{x}_t, t \mid s, \phi_s)$
  $\mathbf{x}_{t+dt} \leftarrow \mathbf{x}_t + \mathbf{v} \cdot dt$
end for
$\hat{\mathbf{r}} \leftarrow \mathbf{x}_1 \cdot \sigma_\mathbf{r} + \mu_\mathbf{r}$ {Denormalize}
$\mathbf{z}_{\text{gen}} \leftarrow \boldsymbol{\mu}_s + \hat{\mathbf{r}}$ {Add centroid}
Evaluate $f_\theta(\mathbf{z}_{\text{gen}}, \cdot)$ on 256^3 grid; extract mesh via Marching Cubes
return Generated watertight mesh

The decoder f_θ and latent code library are trained jointly using two separate Adam optimizers [43] with learning rate 5×10^{-4} for the decoder and 1×10^{-3} for the latent codes, both with default momentum parameters $\beta_1 = 0.9$, $\beta_2 = 0.999$. Both learning rates are decayed by a factor of 0.5 every 500 epochs via a step scheduler. Training runs for 2,000 epochs with batch size 16,384 SDF query points sampled uniformly across all specimens. The latent regularization weight is $\alpha = 1 \times 10^{-3}$ and the phylogenetic consistency loss weight is $\beta = 5 \times 10^{-3}$.

PhyloFlowNet, the velocity network used within the Residual Conditional Flow Matching stage of the broader PhyloSDF framework, is trained using AdamW [44] with learning rate 1×10^{-4} and weight decay 1×10^{-5}. The learning rate follows a cosine annealing schedule decaying to a minimum of 1×10^{-6} over 10,000 epochs, with batch size 256. The variance preservation penalty weight is $\lambda_v = 0.1$ and CFG dropout probability is $p_{\text{drop}} = 0.05$. During training, the species conditioning is randomly replaced with a null token with probability p_{drop}, so that at generation time the velocity can be interpolated between conditional and unconditional predictions to control sample quality versus diversity. All experiments use a single NVIDIA GPU. Latent codes are initialized from $\mathcal{N}(0, 0.01^2)$. The random seed is fixed to 42 for reproducibility.

The velocity network v_θ is a 3-layer residual MLP [45] with 128 hidden units, GELU activations [46], and LayerNorm. Conditioning signals are concatenated with the noisy residual before the input projection: a sinusoidal time embedding (128-dim), species embedding (32-dim, with one additional null-token embedding for CFG), phylogenetic embedding (32-dim via a 2-layer MLP projection from the 32-dim phylo embedding), and bounding-box projection (32-dim). The total parameter count is 283K, deliberately kept small relative to the augmented dataset size.

The detailed layer-by-layer specifications of both networks are provided in the Supporting Information. Table S1 shows the DeepSDF decoder architecture with $D = 64$, and Table S2 shows the PhyloFlowNet velocity network architecture.

S2 Additional Results

In Figure S1, we present a comparison of *G. fuliginosa* skulls generated by Residual CFM and the GMM baseline. In Figure S2, we present a method comparison for intra-species diversity. Figure S3 shows the leave-one-species-out generalization, from which we can see that the centroid error is consistently below within-species variation across all 18 evaluated species.

Table S3 reports the complete LOSO results for all 18 eligible species, including the three nearest phylogenetic neighbors used for centroid prediction, the centroid prediction error, the true within-species spread, and the generalization ratio. The per-species results confirm that generalization performance correlates with phylogenetic embeddedness: species within densely sampled genera (e.g., *Geospiza*, *Loxigilla*) consistently

achieve ratios below 1.27×, while the phylogenetically isolated *P. crassirostris* yields the highest ratio of 1.46×.

Table S4 consolidates all evaluation metrics for the final Residual CFM model into a single reference table, including fidelity, coverage, distributional distances, phylogenetic consistency, generativity verification scores, and reconstruction quality.

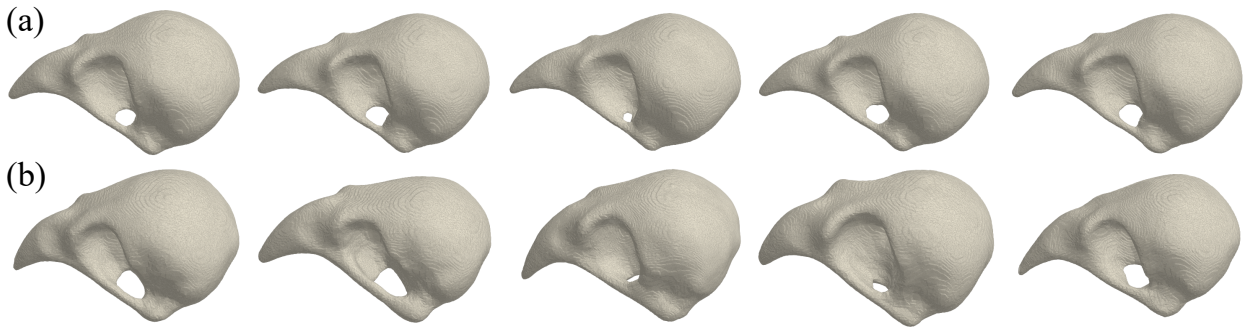

Figure S1: **Comparison of *G. fuliginosa* skulls generated by Residual CFM (row a, $n = 5$) and the GMM baseline (row b, $n = 5$).** CFM samples are geometrically consistent with the *G. fuliginosa* morphotype across all five outputs: beak shape, cranial vault curvature, and overall skull proportions remain stable, reflecting its superior fidelity (NN-CD 0.00181 vs. 0.00190). GMM samples exhibit greater within-row shape variation, including pronounced differences in beak length and cranial depth, consistent with its higher mesh-level diversity score (27.6% vs. 5.2% of real intra-species variation). However, several GMM outputs display anatomically atypical beak geometries and surface artifacts, indicating that the unconstrained Gaussian fit places non-negligible probability mass outside the biologically plausible region of morphospace.

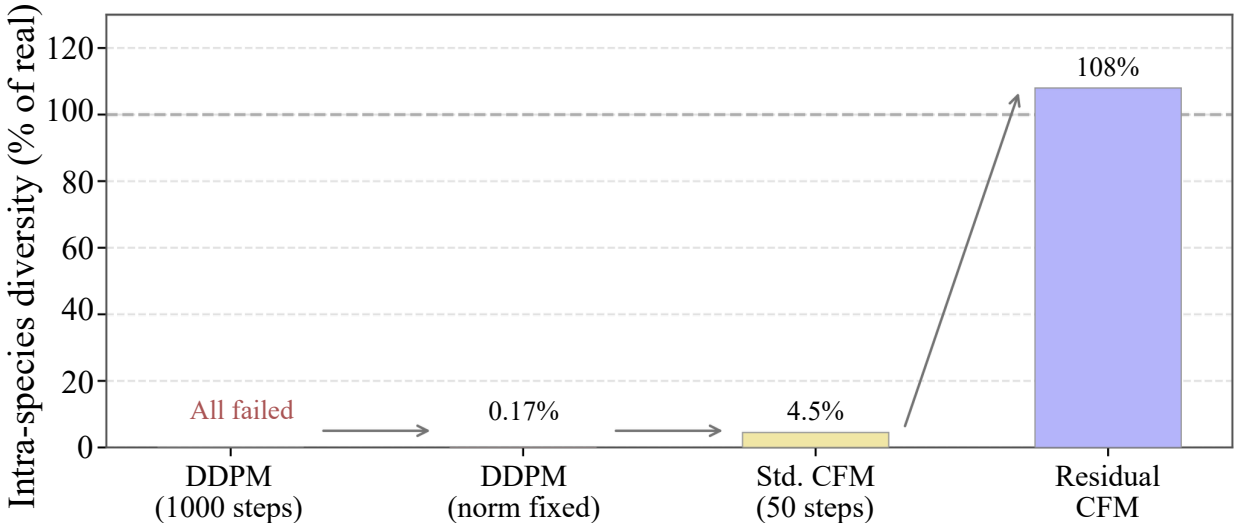

Figure S2: **Method comparison: intra-species diversity.** Only Residual CFM recovers biological-level variation. DDPM fails entirely; standard CFM mode-collapses to centroids; GMM achieves partial diversity.

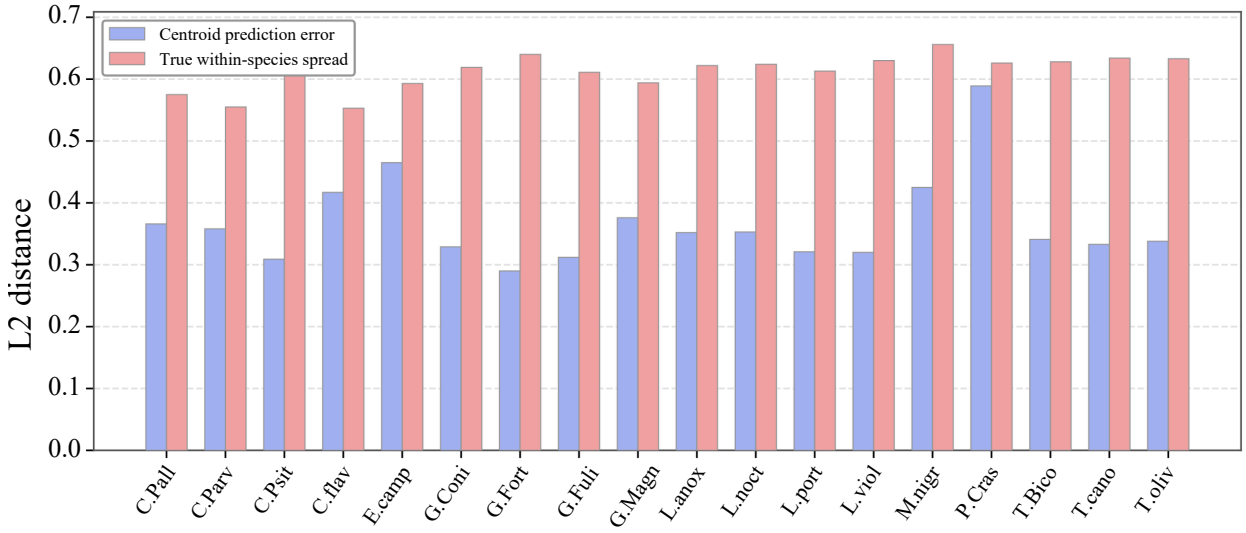

Figure S3: **Leave-one-species-out generalization.** Blue: centroid prediction error (predicted vs. true centroid L_2 distance). Red: true within-species spread. The centroid error is consistently below within-species variation across all 18 evaluated species, confirming that phylogenetic neighbors provide useful positional information for held-out taxa.

Layer	**Input dim**	**Output dim**	**Notes**
Linear 1	$64 + 3 = 67$	512	Weight norm + ReLU
Linear 2–4	512	512	Weight norm + ReLU
Linear 5	$512 + 67 = 579$	512	Skip connection + WN + ReLU
Linear 6–7	512	512	Weight norm + ReLU
Linear 8	512	1	Tanh output

Table S1: DeepSDF decoder architecture ($D = 64$).

Component	**Dim**	**Params**	**Notes**
Sinusoidal time embed	$\rightarrow 128$	33K	2-layer MLP
Species embedding	$25 \rightarrow 32$	800	24 species + 1 null (CFG)
Phylo projection	$32 \rightarrow 32$	4.2K	2-layer MLP
Size projection	$3 \rightarrow 32$	1.2K	2-layer MLP
Input projection	$288 \rightarrow 128$	37K	Linear
Residual blocks ($\times 3$)	128	198K	LayerNorm + GELU + Dropout(0.05)
Output projection	$128 \rightarrow 64$	8.5K	LayerNorm + Linear
Total		**283K**	

Table S2: PhyloFlowNet velocity network architecture.

Species	n	**Nearest neighbors**	**Centroid err.**	**Within-sp.**	**Ratio**
C. pallidus	4	*C. parvulus*, *C. psittacula*, *C. flaveola*	0.366	0.575	1.33×
C. parvulus	5	*C. pallidus*, *C. psittacula*, *C. flaveola*	0.358	0.555	1.36×
C. psittacula	4	*C. pallidus*, *C. parvulus*, *C. flaveola*	0.309	0.675	1.12×
C. flaveola	5	*C. pallidus*, *C. parvulus*, *C. psittacula*	0.417	0.553	1.39×
E. campestris	5	*L. anoxanthus*, *L. noctis*, *L. portoricensis*	0.465	0.593	1.35×
G. conirostris	7	*G. difficilis*, *G. fortis*, *G. fuliginosa*	0.329	0.619	1.24×
G. fortis	5	*G. conirostris*, *G. difficilis*, *G. fuliginosa*	0.290	0.640	1.13×
G. fuliginosa	6	*G. conirostris*, *G. difficilis*, *G. fortis*	0.312	0.611	1.21×
G. magnirostris	5	*G. conirostris*, *G. difficilis*, *G. fortis*	0.376	0.594	1.27×
L. anoxanthus	5	*L. noctis*, *L. portoricensis*, *L. violacea*	0.352	0.622	1.21×
L. noctis	4	*L. anoxanthus*, *L. portoricensis*, *L. violacea*	0.353	0.624	1.23×
L. portoricensis	5	*L. anoxanthus*, *L. noctis*, *L. violacea*	0.321	0.613	1.20×
L. violacea	5	*L. anoxanthus*, *L. noctis*, *L. portoricensis*	0.320	0.630	1.16×
M. nigra	4	*E. campestris*, *L. anoxanthus*, *L. noctis*	0.425	0.656	1.23×
P. crassirostris	4	*C. pallidus*, *C. parvulus*, *C. psittacula*	0.589	0.626	1.46×
T. bicolor	5	*T. canora*, *T. olivacea*, *E. campestris*	0.341	0.628	1.18×
T. canora	5	*T. bicolor*, *T. olivacea*, *E. campestris*	0.333	0.634	1.22×
T. olivacea	4	*T. bicolor*, *T. canora*, *E. campestris*	0.338	0.633	1.19×
Mean			**0.361**	**0.619**	**1.25×**

Table S3: LOSO results for all 18 species with ≥ 4 specimens. Ratio = Gen-NN / Within-held-out (lower is better).

Metric	**Value**
Chamfer Distance (mean ± std)	5.914 ± 0.038
Coverage	0.53
MMD	9.767
Latent Phylogenetic Consistency (r)	0.993
Morphometric PCA overlap	0.008
Morphometric Fréchet Distance (CFM)	10,641
Morphometric Fréchet Distance (GMM)	13,322
Memorized meshes	0 / 180
Residual meaningfulness	42.0%
Novelty ratio	26.4%
Reconstruction CD (mean / median)	0.0022 / 0.0004

Table S4: Complete evaluation metrics for the final Residual CFM model.